

Dove prism based rotating dual beam bidirectional Doppler OCT

Cedric Blatter, Séverine Coquoz, Branislav Grajciar, Amardeep S. G. Singh, Marco Bonesi, René M. Werkmeister, Leopold Schmetterer, and Rainer A. Leitgeb*

Center of Medical Physics and Biomedical Engineering,
Medical University Vienna, Waehringer Guertel 18-20, 1090 Vienna, Austria
*rainer.leitgeb@meduniwien.ac.at

Abstract: Traditional Doppler OCT is highly sensitive to motion artifacts due to the dependence on the Doppler angle. This limits its accuracy in clinical practice. To overcome this limitation, we use a bidirectional dual beam technique equipped with a novel rotating scanning scheme employing a Dove prism. The volume is probed from two distinct illumination directions with variable controlled incidence plane, allowing for reconstruction of the true flow velocity at arbitrary vessel orientations. The principle is implemented with Swept Source OCT at 1060nm with 100,000 A-Scans/s. We apply the system to resolve pulsatile retinal absolute blood velocity by performing segment scans around the optic nerve head and circumpapillary scan time series.

©2013 Optical Society of America

OCIS codes: (170.4500) Optical coherence tomography; (110.4500) Optical coherence tomography; (170.2655) Functional monitoring and imaging; (280.2490) Flow diagnostics.

References and links

1. W. Drexler and J. G. Fujimoto, *Optical Coherence Tomography—Technology and Applications* (Springer, 2008).
2. R. A. Leitgeb, “Current technologies for high speed and functional imaging with optical coherence tomography,” in *Advances in Imaging and Electron Physics*, Volume 168: Optics of Charged Particle Analyzers, P. W. Hawkes, ed. (Elsevier, 2011), Chap. 3.
3. S. Yazdanfar, A. M. Rollins, and J. A. Izatt, “In vivo imaging of human retinal flow dynamics by color Doppler optical coherence tomography,” *Arch. Ophthalmol.* **121**(2), 235–239 (2003).
4. Z. Ding, Y. Zhao, H. Ren, J. S. Nelson, and Z. Chen, “Real-time phase-resolved optical coherence tomography and optical Doppler tomography,” *Opt. Express* **10**(5), 236–245 (2002).
5. V. Yang, M. Gordon, B. Qi, J. Pekar, S. Lo, E. Seng-Yue, A. Mok, B. Wilson, and I. Vitkin, “High speed, wide velocity dynamic range Doppler optical coherence tomography (Part I): System design, signal processing, and performance,” *Opt. Express* **11**(7), 794–809 (2003).
6. R. A. Leitgeb, L. Schmetterer, W. Drexler, A. F. Fercher, R. J. Zawadzki, and T. Bajraszewski, “Real-time assessment of retinal blood flow with ultrafast acquisition by color Doppler Fourier domain optical coherence tomography,” *Opt. Express* **11**(23), 3116–3121 (2003).
7. N. Nassif, B. Cense, B. Hyle Park, S. H. Yun, T. C. Chen, B. E. Bouma, G. J. Tearney, and J. F. de Boer, “In vivo human retinal imaging by ultrahigh-speed spectral domain optical coherence tomography,” *Opt. Lett.* **29**(5), 480–482 (2004).
8. J. Zhang and Z. Chen, “In vivo blood flow imaging by a swept laser source based Fourier domain optical Doppler tomography,” *Opt. Express* **13**(19), 7449–7457 (2005).
9. B. Rao, L. F. Yu, H. K. Chiang, L. C. Zacharias, R. M. Kurtz, B. D. Kuppermann, and Z. P. Chen, “Imaging pulsatile retinal blood flow in human eye,” *J. Biomed. Opt.* **13**(4), 040505 (2008).
10. T. Schmoll, C. Kolbitsch, and R. A. Leitgeb, “Ultra-high-speed volumetric tomography of human retinal blood flow,” *Opt. Express* **17**(5), 4166–4176 (2009).
11. I. Grulkowski, I. Gorczynska, M. Szkulmowski, D. Szlag, A. Szkulmowska, R. A. Leitgeb, A. Kowalczyk, and M. Wojtkowski, “Scanning protocols dedicated to smart velocity ranging in spectral OCT,” *Opt. Express* **17**(26), 23736–23754 (2009).
12. J. E. Grunwald, C. E. Riva, J. Baine, and A. J. Brucker, “Total retinal volumetric blood flow rate in diabetic patients with poor glycemic control,” *Invest. Ophthalmol. Vis. Sci.* **33**(2), 356–363 (1992).
13. G. Garhofer, R. Werkmeister, N. Dragostinoff, and L. Schmetterer, “Retinal blood flow in healthy young subjects,” *Invest. Ophthalmol. Vis. Sci.* **53**(2), 698–703 (2012).
14. C. E. Riva, M. Geiser, and B. L. Petrig, “Ocular blood flow assessment using continuous laser Doppler flowmetry,” *Acta Ophthalmol. (Copenh.)* **88**(6), 622–629 (2010).
15. J. P. Garcia, Jr., P. T. Garcia, and R. B. Rosen, “Retinal blood flow in the normal human eye using the canon laser blood flowmeter,” *Ophthalmic Res.* **34**(5), 295–299 (2002).

16. D. Schmidl, A. Boltz, S. Kaya, M. Lasta, B. Pemp, G. Fuchsjäger-Mayrl, A. Hommer, G. Garhofer, and L. Schmetterer, "Role of nitric oxide in optic nerve head blood flow regulation during isometric exercise in healthy humans," *Invest. Ophthalmol. Vis. Sci.* **54**(3), 1964–1970 (2013).
17. R. Michaely, A. H. Bachmann, M. L. Villiger, C. Blatter, T. Lasser, and R. A. Leitgeb, "Vectorial reconstruction of retinal blood flow in three dimensions measured with high resolution resonant Doppler Fourier domain optical coherence tomography," *J. Biomed. Opt.* **12**(4), 041213–041217 (2007).
18. S. Makita, T. Fabritius, and Y. Yasuno, "Quantitative retinal-blood flow measurement with three-dimensional vessel geometry determination using ultrahigh-resolution Doppler optical coherence angiography," *Opt. Lett.* **33**(8), 836–838 (2008).
19. Y. M. Wang, B. A. Bower, J. A. Izatt, O. Tan, and D. Huang, "Retinal blood flow measurement by circumpapillary Fourier domain Doppler optical coherence tomography," *J. Biomed. Opt.* **13**(6), 064003 (2008).
20. Y. M. Wang, A. A. Fawzi, R. Varma, A. A. Sadun, X. B. Zhang, O. Tan, J. A. Izatt, and D. Huang, "Pilot study of optical coherence tomography measurement of retinal blood flow in retinal and optic nerve diseases," *Invest. Ophthalmol. Vis. Sci.* **52**(2), 840–845 (2011).
21. A. S. Singh, C. Kolbitsch, T. Schmoll, and R. A. Leitgeb, "Stable absolute flow estimation with Doppler OCT based on virtual circumpapillary scans," *Biomed. Opt. Express* **1**(4), 1047–1058 (2010).
22. V. J. Srinivasan, S. Sakadžić, I. Gorczynska, S. Ruvinskaya, W. C. Wu, J. G. Fujimoto, and D. A. Boas, "Quantitative cerebral blood flow with optical coherence tomography," *Opt. Express* **18**(3), 2477–2494 (2010).
23. B. Baumann, B. Potsaid, M. F. Kraus, J. J. Liu, D. Huang, J. Hornegger, A. E. Cable, J. S. Duker, and J. G. Fujimoto, "Total retinal blood flow measurement with ultrahigh speed swept source/Fourier domain OCT," *Biomed. Opt. Express* **2**(6), 1539–1552 (2011).
24. W. Choi, B. Baumann, J. J. Liu, A. C. Clermont, E. P. Feener, J. S. Duker, and J. G. Fujimoto, "Measurement of pulsatile total blood flow in the human and rat retina with ultrahigh speed spectral/Fourier domain OCT," *Biomed. Opt. Express* **3**(5), 1047–1061 (2012).
25. T. Schmoll and R. A. Leitgeb, "Heart-beat-phase-coherent Doppler optical coherence tomography for measuring pulsatile ocular blood flow," *J. Biophotonics* **6**(3), 275–282 (2013).
26. Y.-C. Ahn, W. Jung, and Z. Chen, "Quantification of a three-dimensional velocity vector using spectral-domain Doppler optical coherence tomography," *Opt. Lett.* **32**(11), 1587–1589 (2007).
27. C. J. Pedersen, D. Huang, M. A. Shure, and A. M. Rollins, "Measurement of absolute flow velocity vector using dual-angle, delay-encoded Doppler optical coherence tomography," *Opt. Lett.* **32**(5), 506–508 (2007).
28. B. H. Park, M. C. Pierce, B. Cense, S. H. Yun, M. Mujat, G. J. Tearney, B. E. Bouma, and J. F. de Boer, "Real-time fiber-based multi-functional spectral-domain optical coherence tomography at 1.3 μm ," *Opt. Express* **13**(11), 3931–3944 (2005).
29. N. V. Iftimia, D. X. Hammer, R. D. Ferguson, M. Mujat, D. Vu, and A. A. Ferrante, "Dual-beam Fourier domain optical Doppler tomography of zebrafish," *Opt. Express* **16**(18), 13624–13636 (2008).
30. R. M. Werkmeister, N. Dragostinoff, M. Pircher, E. Götzinger, C. K. Hitzenberger, R. A. Leitgeb, and L. Schmetterer, "Bidirectional Doppler Fourier-domain optical coherence tomography for measurement of absolute flow velocities in human retinal vessels," *Opt. Lett.* **33**(24), 2967–2969 (2008).
31. R. M. Werkmeister, N. Dragostinoff, S. Palkovits, R. Told, A. Boltz, R. A. Leitgeb, M. Gröschl, G. Garhöfer, and L. Schmetterer, "Measurement of absolute blood flow velocity and blood flow in the human retina by dual-beam bidirectional Doppler Fourier-domain optical coherence tomography," *Invest. Ophthalmol. Vis. Sci.* **53**(10), 6062–6071 (2012).
32. R. M. Werkmeister, S. Palkovits, R. Told, M. Gröschl, R. A. Leitgeb, G. Garhöfer, and L. Schmetterer, "Response of retinal blood flow to systemic hyperoxia as measured with dual-beam bidirectional Doppler Fourier-domain optical coherence tomography," *PLoS ONE* **7**(9), e45876 (2012).
33. H. C. Hendargo, R. P. McNabb, A.-H. Dhalla, N. Shepherd, and J. A. Izatt, "Doppler velocity detection limitations in spectrometer-based versus swept-source optical coherence tomography," *Biomed. Opt. Express* **2**(8), 2175–2188 (2011).
34. B. Považay, B. Hermann, A. Unterhuber, B. Hofer, H. Sattmann, F. Zeiler, J. E. Morgan, C. Falkner-Radler, C. Glittenberg, S. Blinder, and W. Drexler, "Three-dimensional optical coherence tomography at 1050 nm versus 800 nm in retinal pathologies: enhanced performance and choroidal penetration in cataract patients," *J. Biomed. Opt.* **12**(4), 041211 (2007).
35. Y. L. Chen, D. L. Burnes, M. de Bruin, M. Mujat, and J. F. de Boer, "Three-dimensional pointwise comparison of human retinal optical property at 845 and 1060 nm using optical frequency domain imaging," *J. Biomed. Opt.* **14**(2), 024016 (2009).
36. C. E. Riva, G. T. Feke, B. Eberli, and V. Benary, "Bidirectional LDV system for absolute measurement of blood speed in retinal vessels," *Appl. Opt.* **18**(13), 2301–2306 (1979).
37. C. Kolbitsch, T. Schmoll, and R. A. Leitgeb, "Histogram-based filtering for quantitative 3D retinal angiography," *J. Biophotonics* **2**(6-7), 416–425 (2009).
38. P. Meemon and J. P. Rolland, "Swept-source based, single-shot, multi-detectable velocity range Doppler optical coherence tomography," *Biomed. Opt. Express* **1**(3), 955–966 (2010).
39. C. E. Riva, J. E. Grunwald, S. H. Sinclair, and B. L. Petrig, "Blood velocity and volumetric flow rate in human retinal vessels," *Invest. Ophthalmol. Vis. Sci.* **26**(8), 1124–1132 (1985).
40. B. Považay, K. Bizheva, B. Hermann, A. Unterhuber, H. Sattmann, A. Fercher, W. Drexler, C. Schubert, P. Ahnelt, M. Mei, R. Holzwarth, W. Wadsworth, J. Knight, and P. S. J. Russell, "Enhanced visualization of choroidal vessels using ultrahigh resolution ophthalmic OCT at 1050 nm," *Opt. Express* **11**(17), 1980–1986 (2003).

41. B. Braaf, K. A. Vermeer, V. A. D. P. Sicam, E. van Zeeburg, J. C. van Meurs, and J. F. de Boer, "Phase-stabilized optical frequency domain imaging at 1- μm for the measurement of blood flow in the human choroid," *Opt. Express* **19**(21), 20886–20903 (2011).
42. M. Miura, S. Makita, T. Iwasaki, and Y. Yasuno, "An approach to measure blood flow in single choroidal vessel using Doppler optical coherence tomography," *Invest. Ophthalmol. Vis. Sci.* **53**(11), 7137–7141 (2012).
43. T. Schmoll, A. S. Singh, C. Blatter, S. Schriefl, C. Ahlers, U. Schmidt-Erfurth, and R. A. Leitgeb, "Imaging of the parafoveal capillary network and its integrity analysis using fractal dimension," *Biomed. Opt. Express* **2**(5), 1159–1168 (2011).
44. L. An, J. Qin, and R. K. Wang, "Ultrahigh sensitive optical microangiography for in vivo imaging of microcirculations within human skin tissue beds," *Opt. Express* **18**(8), 8220–8228 (2010).
45. D. Y. Kim, J. Fingler, J. S. Werner, D. M. Schwartz, S. E. Fraser, and R. J. Zawadzki, "In vivo volumetric imaging of human retinal circulation with phase-variance optical coherence tomography," *Biomed. Opt. Express* **2**(6), 1504–1513 (2011).
46. A. Mariampillai, B. A. Standish, E. H. Moriyama, M. Khurana, N. R. Munce, M. K. K. Leung, J. Jiang, A. Cable, B. C. Wilson, I. A. Vitkin, and V. X. D. Yang, "Speckle variance detection of microvasculature using swept-source optical coherence tomography," *Opt. Lett.* **33**(13), 1530–1532 (2008).
47. B. Braaf, K. A. Vermeer, K. V. Vienola, and J. F. de Boer, "Angiography of the retina and the choroid with phase-resolved OCT using interval-optimized backstitched B-scans," *Opt. Express* **20**(18), 20516–20534 (2012).
48. C. Blatter, T. Klein, B. Grajciar, T. Schmoll, W. Wieser, R. Andre, R. Huber, and R. A. Leitgeb, "Ultrahigh-speed non-invasive widefield angiography," *J. Biomed. Opt.* **17**(7), 070505 (2012).

1. Introduction

Phase resolved Doppler optical coherence tomography (DOCT) has the unique ability to provide depth resolved blood flow velocity information with high spatial resolution and non-invasively. Measurement of tissue blood flow might lead to a better understanding of vascular diseases and might provide beneficial information for treatment monitoring [1,2]. Accurate *in vivo* evaluation of blood flow velocity has been continuously improved due to increasing acquisition speeds that reduce total measurement time and the effect of motion artifacts [3–11]. High-speed OCT allows for example following flow dynamics over time within individual tissue vessels. Among living tissues, the retina has the easiest accessible vasculature because of low-scattering surrounding layers and the natural transparency of the human eye. Various studies have been performed using Laser Doppler Velocimetry (LDV) or Laser Doppler Flowmetry (LDF) [12–16]. Contrary to DOCT, those methods lack however the capability to easily assess different vascular beds in depth. DOCT allows a selective assessment of blood flow and flow velocity in retinal and choroidal vessels and is therefore a promising candidate for early diagnosis of major eye's posterior segment diseases. Still, standard DOCT has the drawback of being sensitive to motion along the optical axis only, requiring information on the blood vessel orientation to calculate the absolute velocity and to quantitatively extract the blood flow. The absolute flow velocity v and the axial velocity v_a are related to the phase difference $\Delta\phi$ between two A-Scans

$$v = \frac{v_a}{\cos(\alpha)} = \frac{\Delta\phi}{2nkT \cos(\alpha)}, \quad (1)$$

with n the refractive index in tissue, k the central wavenumber, α the vessel angle relative to the optical beam or Doppler angle and T the time difference between two measurements, generally between two successive A-Scans. From Eq. (1), it becomes also evident that for vessels close to 90° , the method becomes highly unstable since the error for the absolute velocity v associated to inaccuracies on the Doppler angle estimation is related to the derivative of $1/\cos(\alpha)$. This tends to infinity for α approaching 90° . Unfortunately, most superficial vascular structures accessible by OCT happen to be arranged in flat vessel bed layers parallel to the surface and thus almost perpendicular to the optical beam ($\alpha \sim 90^\circ$).

Several strategies have been followed to extract the absolute velocity within retinal blood vessels with DOCT. The first type deals with the extraction of the vessel angle from structural OCT tomograms. The vessel orientation can be reconstructed from properly registered 3D volumes [17,18]. Again, the method becomes highly inaccurate for vessels close to perpendicular to the incident beam. Another possibility is to extract the vessel gradient from

adjacent cross sections acquired with arc scans or double circular scans at different scan radii [19,20]. The serial acquisition impairs the angle determination because of patient motion that distorts the scanning pattern and its location. Also, multiple scattering below blood vessels makes its precise axial location difficult. Such precision is particularly required to evaluate velocity in regions with close to horizontal vessels ($\alpha \sim 90^\circ$). These methods might be adequate for abrupt vessels close to the optic nerve head (ONH). The dependence on motion artifacts can be alleviated using the concept of virtual scans in particular. In this case, the complexity is shifted to 3D registration in order to provide a proper reference volume that allows tracking back to exact location of 2D scans [21].

An interesting approach is the direct measurement of flow from *en face* cross sections. Since the velocity and the vessel's surface scale oppositely with $\cos(\alpha)$, the integration of the axial velocity over the vessel *en face* cross section cancels the angle dependence and leads to a direct value of the absolute flow [22]. This method works accurately for steep vessels, like the ones present at the ONH [23,24] because of the well defined vessel cross sections in the *en face* plane. It requires a high-speed OCT platform since the data extraction is based on recorded full volumes. Clearly, even at high speed, the vessels within the volume are scanned sequentially and might exhibit different cardiac pulse phases if large volumes are scanned. The condition can be relaxed by fully synchronizing the acquisition with the pulse cycle [25].

The third strategy focuses on the measurement of the 3D velocity vector using simultaneous multi-beam illumination of the same sample point from different angles. Illumination starting from three different directions allows for direct absolute velocity measurement [26,27]. Apart from an increase complexity, this solution might not be ideal for retinal imaging. First, the sensitivity of each direction is reduced since the total illumination power of the eye is limited due to laser safety considerations. High sensitivity is however desirable since phase noise and the minimum detectable velocity scale with signal-to-noise ratio (SNR) assuming proper lateral sampling [28]. Second, the poor optical quality of the human eye leaves the overlap on the retina of several beams, required for accurate absolute velocity calculation, and its sustenance during the whole measurement challenging. The situation is less critical in case of illumination of the same sample point at two different angles. In this case the vessel angle relative to the incidence plane supported by the two illumination beams is additionally needed to extract the absolute velocity [29,30]. The latter can be easily extracted from an OCT fundus projection. The validity of this configuration was demonstrated *in vivo* by the measurement of venous bifurcations [31] and by comparison with LDV [32]. However the static optical configuration used for previous studies does not allow for measuring every vessel orientation and thus any vessel of the retina. The absolute velocity can basically not be extracted if the incidence plane is perpendicular to the flow direction in the *en face* projection.

In this work, we perform absolute velocity DOCT measurements in the human eye with a flexible scanning dual beam bidirectional system. The two parallel illumination beams are spatially separated at the eye pupil before focused on the same spot on the retina, and the detection is performed via a dual interferometer setup. The system is based on high-speed swept source technology that allows measuring higher flow velocity, closer to the ONH, without any fringe wash-out [33]. Furthermore, 1 μ m central wavelength shows better penetration into the choroid and a better performance when cataract occurs as compared to 800nm [34,35]. We introduce a novel scanning scheme that permits to measure any vessel orientation around the ONH under optimal conditions. Rotation of the illumination plane spanned by both incident beams is performed via a Dove prism. Segment scan DOCT time series (BM-Scans) are acquired at selected locations around the ONH, with optimally adjusted illumination plane parallel to the vessel orientations. To decrease the total measurement duration, circumpapillary (circular) DOCT scan series over time are recorded by rotating the Dove prism synchronously with the galvo scanners. The angle independent velocity dynamics is extracted for specific vessel cross-sections of arteries and veins independent of their orientation. This new scanning scheme is certainly not limited to bidirectional DOCT but has the potential to open new applications in OCT.

2. Methods

2.1 Absolute velocity extraction

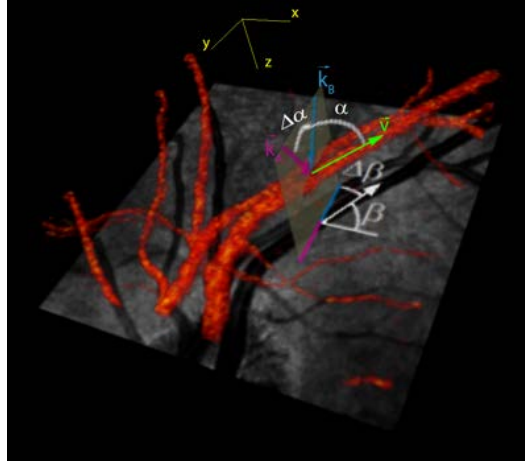


Fig. 1. 3D geometry of the optical illumination. The tissue is illuminated from two different directions (\vec{k}_A and \vec{k}_B) with a separation angle $\Delta\alpha$. Blood vessels (red) have a Doppler angle α between the flow direction \vec{v} and the optical axis z . In the fundus projection (grayscale), vessels have an angle β relative to the scanning coordinates system (x, y) and, in general case, an angle $\Delta\beta$ to the plane formed by \vec{k}_A and \vec{k}_B .

The dual beam bidirectional optical configuration for retinal blood flow assessment was first introduced for LDV [36] and later for OCT [30]. The same sample point is illuminated from two different directions \vec{k}_A and \vec{k}_B . This is achieved by employing two parallel beams that are displaced on the cornea, and then focused on the same spot on the retina. The expression for the absolute velocity in the approximation of a large Doppler angle α is given by:

$$v = \frac{v_a^{(A)} - v_a^{(B)}}{\Delta\alpha \cdot \cos(\Delta\beta)} = \frac{\Delta\phi_A - \Delta\phi_B}{2nkT\Delta\alpha \cdot \cos(\Delta\beta)}, \quad (2)$$

with $\Delta\alpha$ being the separation angle between both direction, $\Delta\beta$ the angle between the illumination plane subtended by the illumination directions \vec{k}_A and \vec{k}_B and the vessel flow direction \vec{v} (Fig. 1). $v_a^{(A,B)}$ are the axial velocities along the illumination directions calculated from the phase differences $\Delta\phi_A$ and $\Delta\phi_B$ according to Eq. (1) respectively. The Doppler angle in this case is taken between the vessel orientation and the optical axis being the resultant vector of the two illuminations. From Eq. (2), it can be seen that the absolute velocity cannot be accurately extracted from both phase difference measurements if $\Delta\beta$ is close to 90° . In this case, both phase differences have similar values so that their difference is dominated by noise and the precise determination of $1/\cos(\Delta\beta)$ is critical because its derivative tends again to infinity. This shortcoming can be eliminated by maintaining a small $\Delta\beta$ (typically $<25^\circ$) for every measurement. Employing a static configuration by modifying the position of the beams in the eye pupil plane is not an option for clinical applications since it requires too much time for adjustment between measurements of different vessels. An elegant dynamic solution is to use a Dove prism. A Dove prism is a truncated right-angle shaped reflective prism that is used usually to invert or in general to rotate an image by an arbitrary angle. In our case, both beams A and B are transmitted through the prism that is spun so that the beam positions are rotated at its exit and in the eye pupil plane (see Fig. 3(a)). Equivalently the angle of the illumination plane on the retina relative to the scanning coordinates system is rotated maintaining thereby $\Delta\beta \sim 0^\circ$ for every probed vessel (see Fig. 3(c)).

This dual angle bidirectional method has the highest accuracy for horizontal vessels (typically for $65^\circ < \alpha < 115^\circ$ with an error smaller than 10%). Out of this range, the approximation of Eq. (2) becomes gradually imprecise and the difference of the phase differences in both channels decreases, mainly because of the small angular separation $\Delta\alpha$ imposed by the limited pupil size. The consequence is that measurements around the optic nerve head need to be performed at a radial distance where vessel inclination is sufficiently small according to the angular range given above to keep the measurement precise.

2.2 Setup

The optical setup of the rotating dual-beam bidirectional OCT system is shown in Fig. 2. The light source is a short cavity swept source operating at 100kA-Scans/s, centered at 1050nm (Axsun Technologies). The source has an optical bandwidth of 110nm with an axial resolution in tissue of 5 μ m. A first fiber coupler (FC) separates the light to the interferometer for beam A and B in red and blue respectively. In the sample arm, both beams are aligned parallel to the optical axis with a defined lateral separation by reflection on a coated right angle prism (M). Displacement of that prism allows for varying the beam separation. Both beams are then transmitted through a Dove prism. The Dove prism can freely rotate around its longitudinal central axis that is aligned with the optical axis. The beams have equal distance to the rotation axis. The continuous rotation is driven by a DC motor in open-loop (DC). The Dove prism has the property to optically rotate an image twice when it mechanically rotates once. For synchronization of the rotation with the OCT system a disk with two opposite slits (see Fig. 3(a)) is mounted on the rotation stage and crosses a light barrier that provides one trigger pulse per optical rotation of the beams. This signal is in particular needed to synchronize the galvo scanners (GVSM002, Thorlabs) with the rotation in the case of circumferential scans (see Fig. 3(b)). The phase between the rotation and the circular scan is adjusted such as to obtain a small $\Delta\beta$ for radial vessels exiting the ONH (see Fig. 3(c)). The beam steering device is aligned so that both beams are symmetrical around the pivot points of the scanner mirrors. The beam separation in the pupil of the eye is ~ 1.6 mm with a beam size of ~ 1.3 mm each. It is currently limited by the scanning mirror aperture and the telescope's (L3,L4) angular magnification of 1.5x. The theoretical spot size on the retina is $\sim 25\mu$ m. In the reference arm, both beams are reflected on the same delay line. The interference is measured with dual-balanced detectors (PDB430C, Thorlabs). The signal is digitalized at 250MSamples/s for each channel with a 12bit analog-to-digital converter (ATS9350, Alazartech). A reference spectrum is acquired with a mirror at the position of the sample and is later used for remapping from wavelength to wavenumber. The total power at the cornea is ~ 1.9 mW, which is consistent with the ANSI standards safe exposure limits. The sensitivity in each channel is ~ 94 dB.

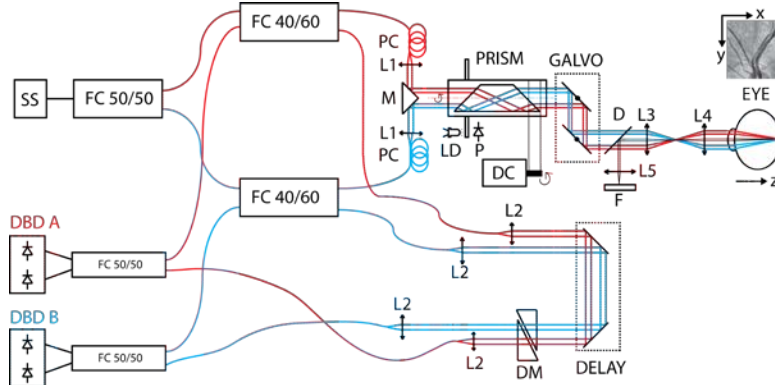


Fig. 2. Optical Setup of the rotating Dove prism based dual-beam bidirectional OCT system. Red: beam A, blue: beam B. SS: Swept source, FC: Fiber coupler, PC: Polarization control, L1 to L5: Lenses, M: Mirror, LD: LED, P: PIN diode, Prism: rotating Dove prism, DC: DC motor, Galvo: Scanning mirrors, D: dichroic mirror, F: fixation screen, DM: Dispersion matching, DBD: Dual-balanced detector.

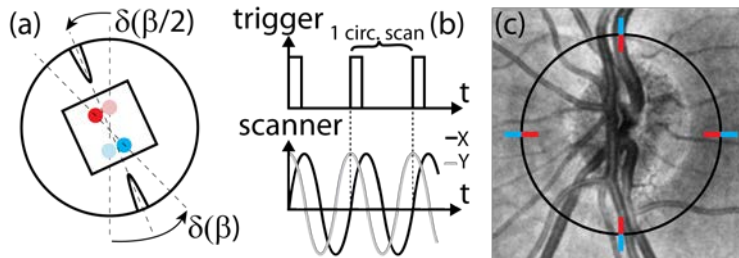


Fig. 3. Synchronisation of the rotation for circular scan. (a) en face (x,y) view at the exit of the Dove prism. The mechanical rotation ($\delta(\beta/2)$) doubles the optical rotation ($\delta(\beta)$). Beam A and B are represented by red and blue disks respectively. Light and saturated colors account for beams at the entrance and exit of the prism respectively. (b) Electrical synchronization between TTL signal derived from the light barrier and scanner driving signals. The light barrier delivers two pulses by Dove prism rotation. (c) Theoretical circular scan location around the ONH. The color lines indicate the rotating incidence plane that allows maintaining small $\Delta\beta$ for every crossed vessel.

3. Results

3.1 In Vitro experiment

We experimentally validate the absolute velocity measurement first *in vitro*. The flow phantom is a capillary of $300\mu\text{m}$, perfused by a solution of one third of milk and two thirds of water moving at constant speed imposed by a pump. The capillary is mounted on a stage allowing for both tilt and rotation and is placed in the focal plane of a lens with 30mm focal length. We measured the velocity in the capillary with varying tilt angles (α) and rotation angles (β) for two preset velocities, using circular scan generated by the galvo scanners and the following two configurations: firstly, when the illuminating beams are static ($\Delta\beta = 90^\circ - \beta$) with the Dove prism at rest (static bidirectional configuration), and secondly, when the beams are rotated by the Dove prism synchronously with the circular scan ($\Delta\beta \sim 0^\circ$).

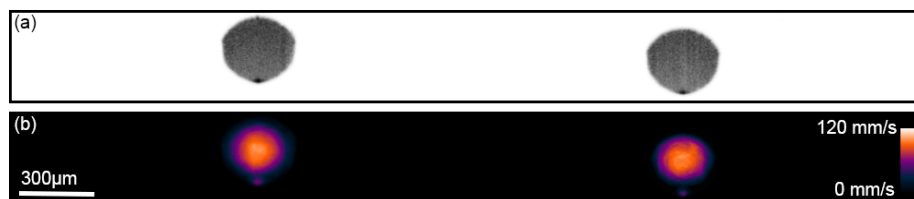


Fig. 4. Representative circular scan of $\sim 2.5^\circ$ diameter crossing the perfused capillary twice. (a) Intensity tomogram. (b) Absolute velocity tomogram. Scale bar is valid for both images.

In both cases, we acquire circular scans time series of twenty scans, each consisting of 6500 A-Scans, with a circular scan frequency of $\sim 15\text{Hz}$ (see Fig. 4). The slight curvature of the capillary cross section due to the circular scan trajectory has no detectable effect on the absolute velocity determination since the radius of the scan is much larger than the capillary diameter. The mean phase difference value for each channel is calculated by averaging the phase difference over the pixels of the capillary open cross section that have a higher intensity than a manually fixed threshold. Prior to the capillary measurement, a bulk phase difference map corresponding to the phase modulation induced by the galvo scanners is acquired by using a paper instead of the capillary. This circular scan angle dependent bulk phase value is then used to correct the capillary flow measurements.

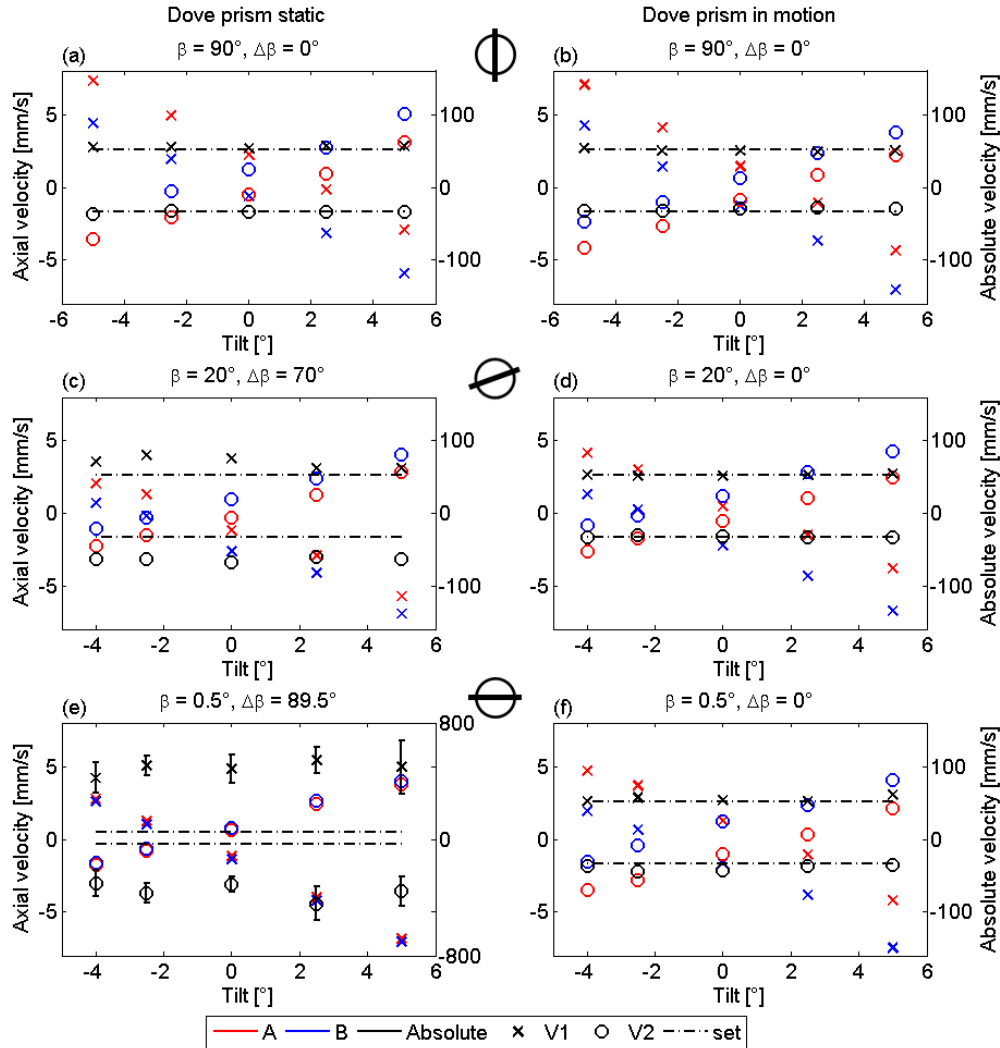


Fig. 5. In vitro measurement with capillary showing the axial velocity (left scale) for channel A (red) and B (blue), as well as the absolute velocity (right scale, black), for different tilt and two different velocities in the capillary, respectively $V1 = 52\text{mm/s}$ (X) and $V2 = -33\text{mm/s}$ (O), compared to the set velocities (dotted line). The left column was measured with static beams, the right with the synchronous rotation. The rows are acquired for different orientations of the capillary: vertical, angled and horizontal, for the top, middle and bottom line respectively (see graphic representation in the middle, where the line and the circle represent the capillary orientation and the circular scan position respectively). The markers represent the average velocity over twenty scans and the error bars show the standard deviation. If not displayed, it is smaller than the marker size, with a relative error of $<3\%$.

Figure 5 shows the results of the *in vitro* experiment. The measurements associated with the velocity in the capillary $V1 = 52\text{mm/s}$ and $V2 = -33\text{mm/s}$ are represented by “X” and “O” respectively. The displayed velocities are averaged over twenty scans. The standard deviation over these scans, when not indicated by error bars, is $<3\%$ of the average velocity. One can clearly see that the single channels A (red) and B (blue) have a strong dependence on the Doppler angle. Their difference, which is proportional to the absolute velocity (shown in black) according to Eq. (2), remains however constant over the tilt range. The absolute velocity has $\sim 5\%$ and $\sim 7\%$ accuracy for the static and dynamic cases, respectively, as calculated from the coefficient of variation of the root-mean-square error (CV(RMSE))

between measured mean and preset velocity in Figs. 5(a) and 5(b). We explain the difference by the limited precision of the pump. Also, for the synchronous rotation in particular, an underestimation of the velocity is possible if there is a slight delay between the rotation of the prism and the circular scan, in that case $\Delta\beta$ cannot be approximated as being zero. Figure 5(c) shows that the static illumination starts to overestimate the absolute velocity, as the difference of both channels becomes smaller. It becomes even more critical in the case when the capillary is placed almost horizontally. Although the phase difference remains approximately constant, the calculated velocity is highly inaccurate as seen from Fig. 5(e). In the case of rotation, an accurate estimation of the velocity is maintained (see Figs. 5(d) and 5(f), CV(RMSE) $\sim 7.5\%$), as compared to the expected high error for the static situation (CV(RMSE) $\sim 64\%$), confirming the validity of our approach.

3.2 *In Vivo* experiment

We measure the blood flow velocity in the retina of a healthy volunteer. The location of measurement is controlled with a fixation target on a display that is presented to the measured eye via a dichroic mirror in the sample arm path. On-line display of the OCT *en face* projection during continuous raster scanning allows fine adjustments by modifying the scanning pattern offset of the galvo scanners. An optimal overlap of both beams on the retina is obtained by adjusting the optical power of the telescope. The position of the beams in the pupil is constantly monitored via a camera. After the optimal measurement position is set, a 3D raster scan centered at the ONH is performed (see Fig. 8(e)). It permits to select the measurement locations for the segment scans, or the optimal radius for circumpapillary scans and to extract the angles of the vessels (β , $\Delta\beta$) from the *en face* mean projection.

The phase difference data for each beam is first processed separately. Because the bulk motion artifacts that add to the galvo scanner phase modulation and to the electronic trigger jitter, are in general unknown, we use a bulk motion algorithm based on histogram analysis to correct for such phase fluctuations [37]. We then use a manual program to segment the vessel cross-sections for both beams in parallel assuming elliptic shapes. The size of the ellipse is set on the phase difference tomogram in the time series that shows the largest flow velocity, i.e. for the systolic pulse phase, and is then kept for every other picture. As for the *in vitro* experiment we calculate the mean velocity over the vessel lumen cross-section. We finally combine the extracted axial velocity information from both channels according to Eq. (2) to obtain the absolute velocity. With the subject's eye length being 23.5mm, as measured with an IOL Master (Zeiss), and taking the spatial separation of the probe beams into account, $\Delta\alpha$ was calculated as $\sim 68\text{mrad}$.

3.2.1 Segment scan

Segment scans series over time, or BM-scans, are acquired at selected locations around the ONH. Each scan consists of 3250 A-Scans and is acquired at a rate of 24Hz. They typically represent 4 to 7°, depending on the number and size of vessels. Because of the limited amount of available RAM, the acquisition is restricted to 75 B-scans or a measurement time of a little more than 3 seconds. The angle of the scan relative to the raster scanning coordinates is set such as to cross the vessels close to perpendicularly. The Dove prism is static but its angular position is adjusted in order to be in the condition of $\Delta\beta \sim 0^\circ$.

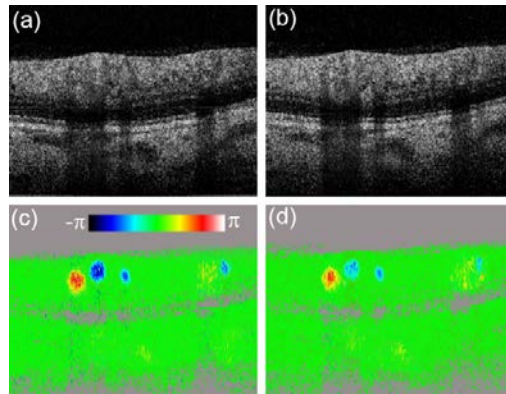


Fig. 6. Representative segment scans of $\sim 7^\circ$ consisting of 3250 A-scans. (a,c): beam A, (b,d): beam B. (a,b): intensity tomograms, (c,d): high dynamic range quantitative Doppler tomograms obtained by combining phase difference values from different A-Scans intervals (1,3 and 4). Scan position is indicated by a dashed white line in Fig. 8(e).

Figure 6 shows a representative segment scan of the time series for beam A and B on the left and right respectively. The top row shows intensity tomograms, while the bottom one shows DOCT or phase differences tomograms later used for quantitative analysis. In order to assess both veins and arteries, we analyze not only the phase difference between successive A-scans (interval 1) but also between the A-scan i and $i + 2$, $i + 3$ and $i + 4$ (respective A-scan intervals 2, 3 and 4). It permits to increase the measurable velocity range without having to deal with phase wrapping and at little cost of phase noise increase if a high oversampling is selected [38]. We typically have increasing phase difference noise of 10, 17, 24 and 38mrad for increasing A-scan interval 1, 2, 3 and 4 respectively. The mean value is calculated over an ellipse of 100×35 pixels positioned at a location without any vessel. Figures 6(c) and 6(d) show high dynamic range Doppler tomograms that are obtained by combining the phase difference information from different intervals (in that case 1, 3 and 4) in the same phase difference scale from $-\pi$ to π . Figure 7 shows the original phase difference images for intervals 1, 3 and 4 of beam B that were used to create the high dynamic range image in Fig. 6(d). The latter figure is obtained from Fig. 7 by manually selecting the flow signatures with highest contrast within the segmented vessel cross sections and merging them into a single phase difference image. The quantitative evaluation is currently performed on constant phase difference interval time series.

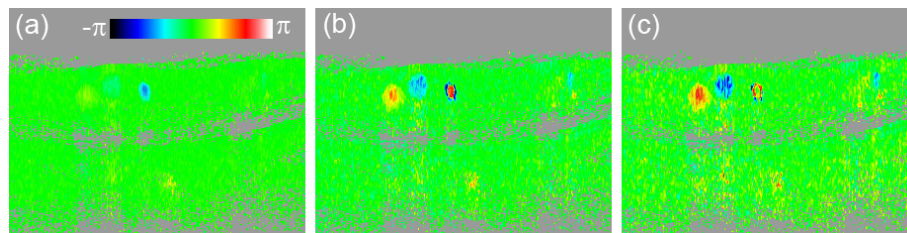


Fig. 7. DOCT segment scans of beam B spanning a range of $\sim 7^\circ$ consisting of 3250 A-scans with phase differences calculated between A-Scans ($i; i + 1$), ($i; i + 3$) and ($i; i + 4$) in (a), (b) and (c) respectively, used to create the high dynamic range DOCT image in Fig. 6(d). Scan position is indicated by a dashed white line in Fig. 8(e).

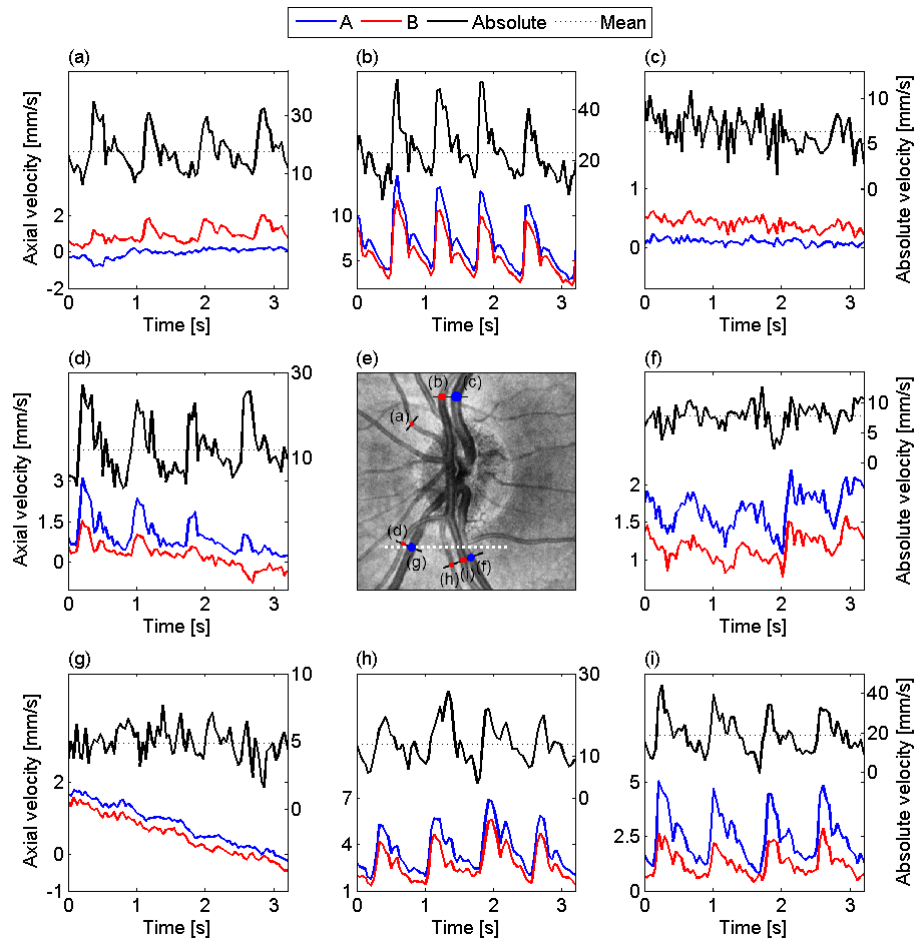


Fig. 8. Blood flow velocity evolution in selected vessels obtained from several segment scan time series. Red and blue represent the axial velocity measured for beam A and B respectively, left scale. It permits to calculate the absolute velocity (black line) and its mean value (dotted line), right scale. (e) is a $\sim 15^\circ$ fundus view centered at the ONH obtained by calculating the en-face mean projection of an OCT 3D data set. The positions of the segment scans are overlaid as black lines. The crossing with blood vessels is indicated by colored circles, red and blue for arteries and veins respectively, and letters that correspond to the surrounding time traces. Position of scans in Fig. 6 and Fig. 7 is indicated by a dashed white line.

We selected eight vessels around the ONH and performed five different segment scans. Figure 8 shows the results of the measurement. Figure 8(e) indicates the location of the scans with a dark line and the crossing with arteries and veins with red and blue circles respectively on a fundus image across $\sim 15^\circ$. The average blood flow velocity over each indicated vessel cross section is then displayed as a function of time in the associated panels in Fig. 8. The velocity scale for the single channel (red and blue for A and B respectively) is shown on the left of each graph and corresponds to the axial velocity. The scale for the absolute velocity (black line) and its mean value over time (dotted line) is shown on the right. The range of mean absolute velocities is in good accordance with what was previously measured with LDV [39]. Although that veins velocity are close to the velocity noise limit of our system, the averaging, performed over the large vessel sizes, provides data with good reproducibility. A potential problem might come from the few available static tissue pixels for a proper bulk motion algorithm correction in presence of large vessels. In this case the flow signatures dominate the histogram and the bulk correction leads to an underestimation of the correct

mean velocity. Generally, one can see a strong pulsatility for arteries and an almost constant velocity for the veins. A small pulsatility of the vein is sometimes visible in the single channels, while it disappears in the higher noise of the absolute channel. The noise of the absolute velocity is indeed slightly larger resulting from taking the difference of both channels. This causes also small differences in pulse shapes between axial and absolute velocity even in regions of low motion influences. The single channels show sometimes drifts (see typically Figs. 8(d) and 8(g) for an artery and a vein), while the absolute channel has a constant baseline. It reveals the advantage of this technique of being stable relative to eye drifts that occur during *in vivo* measurement. Such motion artifacts would be difficult to account for with techniques obtaining the Doppler angle from single intensity tomograms.

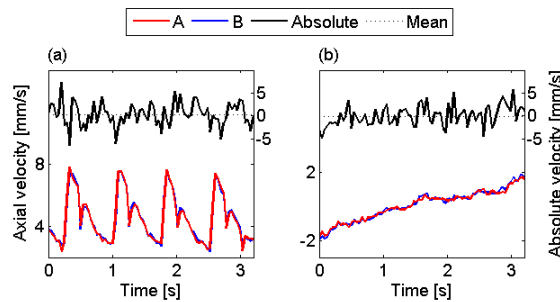


Fig. 9. Deliberate wrong orientation of incidence plane with respect to the vessels leading to an erroneous calculation of the blood flow velocity evolution for an artery and a vein in (a) and (b) respectively. Red and blue represent the axial velocity (left scale) measured for beam A and B respectively. $\Delta\beta$ was set to 90° and the absolute velocity (black line) and its mean value (dotted line) (right scale) were not scaled by the $\cos(\Delta\beta)$ factor in Eq. (2).

In order to demonstrate the advantage of being able to rotate the illumination plane for optimal measurement conditions, we show the negative effect by deliberately rotating the plane such that $\Delta\beta \sim 90^\circ$. Figure 9 shows the obtained results for (a) an artery and (b) a vein. As expected, the difference of both phase differences is close to zero, and both channels are measuring basically the same signal. As a result, the determination of the absolute velocity becomes inaccurate. Furthermore in that case, the velocity was not scaled considering the factor $\cos(\Delta\beta)$ in Eq. (2), which would in addition increase the imprecision.

3.2.2 Circumpapillary scan

The advantages of the segment scan over the circular scan are numerous. Firstly, the measurement location and the illumination plane orientation can be freely chosen for a segment scan while it is fixed by the radius and the center of the circular scan. Secondly, the smaller scan amplitude that can be achieved with a segment scan allows for a better sampling of a single vessel as compared to a circular scan. It is then possible to average over more points leading to an overall smaller phase noise. Furthermore short segment scans are less affected by global ocular aberrations that might cause loss of overlap between both beams.

Nevertheless, circular scans still have an important justification: the measurement time to assess all large vessels around the ONH is significantly reduced. In particular for our bidirectional DOCT platform, the orientation of the incidence plane can be dynamically adjusted without user intervention. We take advantage of the fact that most blood vessels in proximity of the ONH are close to radially oriented and, thus, are crossed perpendicularly by a circular scan. In case of a circumpapillary scan, β is almost a continuous function from 0 to -360° . In order to maintain $\Delta\beta \sim 0^\circ$ for every vessel, the Dove prism is simply rotated synchronously with the beam steering device. The position of both beams in the pupil thus rotates while being static in the case of segment scans.

Each-scan consists of 6500 A-Scans. The rotation frequency of the Dove prism corresponds then to ~ 7.5 Hz resulting in a circular scan frequency of 15 Hz. The circular scan

has a diameter of $\sim 9^\circ$ centered at the ONH. The series consists of 32 scans for measurement duration of slightly more than 2 seconds.

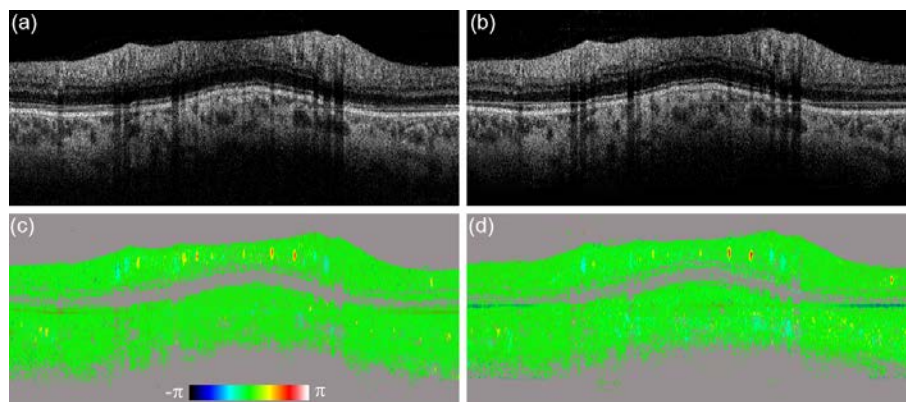


Fig. 10. Representative circumpapillary scans at the ONH spanning $\sim 9^\circ$ diameter and consisting of 6500 A-scans. (a,c): beam A, (b,d): beam B. (a,b): intensity tomograms, (c,d): high dynamic range quantitative Doppler tomograms obtained by combining vessel value from phase difference between successive A-Scans and between A-Scan i and $i + 2$.

Figure 10 shows a representative circumpapillary scan of the time series for beam A and B on the left and right respectively. The theoretical location of the scans is indicated by a dark line, the start and direction of rotation with the arrow in Fig. 11(e). The top row shows intensity tomograms, while the bottom one shows DOCT tomograms later used for quantitative analysis. In the case of circular scans, we typically have phase noise of 10 mrad, and 21mrad for phase difference A-scan interval 1 and 2. The mean value is again calculated over an ellipse of 100x35 pixels positioned at a location without any vessel. Figures 10(c) and 10(d) show high dynamic range Doppler tomogram that are obtained by combining the phase difference information from different A-scan intervals (in that case 1 and 2).

Figure 11 shows the results of the analysis of the same vessels and the same volunteer as for Fig. 8. The start of rotation is selected to be in a region with absence of large vessels. Similar time traces as in Fig. 8 are measured. A higher fluctuation is however visible and comes from the smaller time sampling and the fact that the average is calculated over less spatial sampling points of the vessel cross section. The signal shown in Fig. 11 is averaged by means of a moving window over two time points. The mean velocity values are slightly higher than the ones obtained with the segment scans. Since every measured value is higher, we believe that this can be attributed to different physiological conditions of the volunteer at the different measurement time of the day.

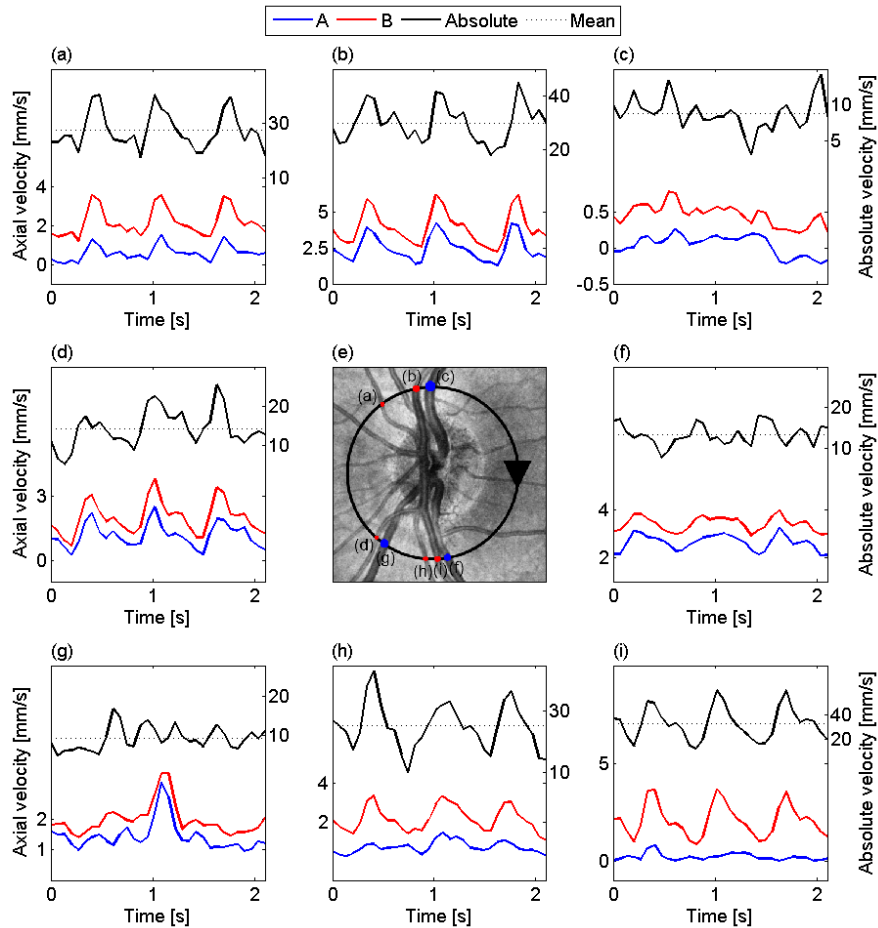


Fig. 11. Blood flow velocity evolution in selected vessels obtained by a circumpapillary scan. Red and blue represent the axial velocity measured for beam A and B respectively. It permits to calculate the absolute velocity (black line) and its mean value (dotted line). The traces were averaged over two points. (e) is a $\sim 15^\circ$ fundus view centered at the ONH obtained by calculating the *en face* mean projection of an OCT 3D data set. The black circle indicates the theoretical position and shape of the $\sim 9^\circ$ diameter circumpapillary scan. The black arrow shows the direction and start position of rotation. The crossing with blood vessels is indicated by colored circles, red and blue for arteries and veins respectively, and letters that correspond to the surrounding time traces.

3.2.3 Choroidal blood flow velocity

Having a Doppler OCT platform operating at the longer central wavelength of 1060nm is predestined to assess also choroidal flow signatures [40–42]. The choroid is the main oxygen and nutrients supplier of the outer retina, its assessment would therefore promise a more complete picture of retinal health. Figure 12 shows the quantitative evaluation of a choroidal vessel, based on the acquisition of a segment scan time series, each consisting of 3250A-Scans over $\sim 3^\circ$. In Fig. 12(a), the DOCT phase difference velocity profile (color lookup table) is overlaid on the structural information (grayscale). The quantitative absolute velocity and its mean value, in solid and dotted dark lines, are calculated by scaling the difference of the axial velocities, red and blue for channels A and B, respectively. Again, a drift is visible in the single channels while absent in the calculated absolute velocity. The absence of strong pulsatility suggests that this vessel is a vein. The challenge associated to the choroidal network comes from its strong tortuosity. Proper beam overlap becomes of paramount

importance. Also, along with motion, β will rapidly change, making the condition of small $\Delta\beta$ difficult to maintain. Improvement and further quantitative analysis of the choroidal vasculature network is an on-going work.

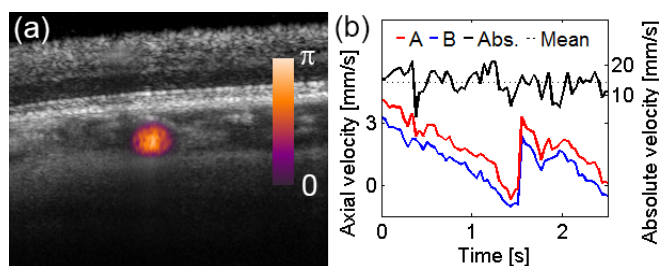


Fig. 12. Quantitative choroidal blood flow velocity analysis. (a) Segment scan of $\sim 3^\circ$ consisting of 3250 A-Scans. The Doppler channel (colored lookup table) is overlaid on the structural information (grayscale). (b) Quantitative analysis of the scan time series. The axial velocity (left scale) for single channels is shown in red and blue for A and B respectively and the absolute velocity (continuous line, right scale) and its mean value (dotted line) in black. The single channels show a drift that is absent from the absolute velocity. The absence of strong pulsatility suggests that this vessel is a vein.

4. Discussion

The dual beam bidirectional technique is a reliable method to calculate the absolute blood flow velocity directly from simultaneously acquired Doppler signals, without the need for Doppler angle extraction from intensity tomograms. It is globally stable towards drifts that occur during *in vivo* measurement. There are however several requirements for this technique to provide accurate results. Firstly, the Doppler angle has to be close to 90° . This condition is generally encountered for tissue imaging since vessels are usually organized in layers parallel to accessible surfaces. In the human eye, only the region inside and close to the optic disk should be avoided. A large beam separation angle, i.e. $\Delta\alpha$ in Eq. (2), would relax this condition, this angle is however limited for retinal imaging by the pupil size of the eye. Secondly, both beams need to measure the same spatial location at the same time. The slight temporal shift introduced by a possible spatial separation of the beams is negligible with respect to the pulse propagation velocity. The spatial overlap is anyway required because of high single axial velocity sensitivity on vessel orientation; already a 1° difference on the Doppler angle α can produce tremendous phase differences (see Fig. 5). The overlap is especially critical in the presence of ocular aberrations. We correct defocus by adapting the telescope optical power to the subject's eye and confirm the overlap by analyzing the vessels position in the tomogram of single channels. A live camera fundus view would be beneficial to confirm the overlap of both beams. Higher aberrations (astigmatism for example) could be corrected by introducing an appropriate optical element between the telescope and the eye. The third requirement for the bidirectional Doppler OCT method is the precise knowledge of the vessel's angle $\Delta\beta$ in the fundus plane. To maintain optimal measurement conditions, we introduced the Dove prism to control the relative angle between illumination plane and vessel. By dynamically rotating the prism, a circular scan with optimal orientation of the incidence plane with respect to all the large radial vessels around the ONH can be performed. Depending on the subject vessel anatomy, the condition $\Delta\beta \sim 0^\circ$ cannot be met for every vessel, however, the angular deviations can be obtained from a fundus view and, thus, be corrected for. For strong vessel tortuosity, several acquisitions with different parameters might be needed.

Currently, the evaluation of the absolute velocity assumes that $\Delta\beta$ remains constant during the time series. It is then advantageous to operate close to the $\Delta\beta \sim 0^\circ$ condition, such as small variations in $\Delta\beta$ are usually negligible for the calculation of the absolute velocity. If the condition cannot be met, the tomogram can still be located in a registered 3D reference volume [21] such as to determine the $\Delta\beta$ values for each scan if necessary.

A major factor that accounts for the limited method precision is the small angular separation between both beams. It has the positive effect that phase wrapping is encountered only at larger velocities. However, since the absolute velocity scales inversely with that value, it increases the absolute minimum detectable velocity as compared to axial one. This is visible in the different measurements above. Increasing slightly the beam separation in the pupil comes at the cost of higher aberrations that might distort the beam overlap. A way to reduce the absolute minimum detectable velocity is increased averaging. This is possible with segment scans but difficult with the circumpapillary scan because the time sampling has to remain small enough to resolve the cardiac pulse cycle and the scan radius large enough to account for the vessels geometry.

The visualization of the microvasculature and assessment of its integrity has also important diagnostic value. In nowadays clinical praxis fluorescein and indocyanine green angiography are used for examination of retinal and choroidal circulation. However, these methods require injection of dye, which might have some adverse effects. A non-invasive measurement based on OCT might, in certain cases, be a favorable alternative while providing complementary depth information. Microvascular contrast can either be obtained directly from intensity images [43] or, more efficiently, by acquiring several tomograms at the same location and calculating motion induced changes, either in the amplitude and/or in the phase of the interference [44–47]. Both, widefield angiograms of the retinal and choroidal vasculatures, as well as smaller field of view resolving capillary layers can be acquired with the same system in a few seconds [48]. 3D vasculature maps allow also a proper planning of optimal blood flow velocity measurement parameters and scanning locations. Finally, a combination of both contrasting and quantitative methods is particularly apt in giving a more complete view of the tissue health as well as treatment success.

5. Conclusion

We introduce a novel scanning scheme based on a Dove prism to improve the flexibility of dual beam bidirectional DOCT measurements. We demonstrate its advantages by comparing static and improved scanning scheme with *in vitro* experiments. We apply our system to human eye for quantitative assessment of retinal and choroidal blood flow velocity dynamics. Segment scans allow for accurate velocity determination of any selected vessel. Circumpapillary scan with synchronous Dove prism rotation permits a rapid absolute velocity extraction of major large vessels around the optic nerve head. The focus of future research will be further improvement of the method regarding the reproducibility of choroidal flow measurements. We believe that the unique feature of contrast vasculature non-invasively as well as providing depth resolved quantitative perfusion values will improve the diagnostic value and acceptance of modern Doppler OCT in clinical practice.

Acknowledgments

We acknowledge financial support from the European Commission Seventh Framework Programme (FP7) HEALTH program (grant 201880, FUN OCT), the Austrian Science Foundation (FWF, Project No. APP21570FW), the Austrian Research Promotion Agency (FFG, Project FA 607A0502) and the Christian Doppler Laboratory for Laser Development and their Application in Medicine.